Diverse dynamics of glutamatergic input underlie heterogeneous response patterns of olfactory bulb mitral and tufted cells *in vivo*

Andrew K. Moran[1,2], Thomas P. Eiting[2], Matt Wachowiak[2]

[1]Interdepartmental Program in Neuroscience, [2]Department of Neurobiology and Anatomy, University of Utah School of Medicine, Salt Lake City, UT

Correspondence to be sent to: Matt Wachowiak, Department of Neurobiology and Anatomy, University of Utah, Salt Lake City, UT, USA. email: matt.wachowiak@utah.edu

ABSTRACT

In vertebrates, olfactory sensory neuron (OSN) activation drives glutamatergic excitation of mitral/tufted (MT) cells and juxtaglomerular interneurons in the olfactory bulb (OB). MT cells show diverse temporal response patterns to odorant stimulation, which have been attributed largely to processing by inhibitory circuits. However, this diversity could reflect differences in the temporal dynamics of excitatory input to MT cells. Here, we imaged odorant-evoked glutamate transients onto MT cell dendrites in the OB of anesthetized and awake mice using the glutamate sensors iGluSnFR and SF-iGluSnFR, allowing us to visualize the dynamics of excitatory synaptic inputs onto MT cells in anesthetized and awake mice. We found a surprising amount of diversity in the temporal dynamics of glutamatergic input to MT cells, both within and across successive odorant inhalations. Response patterns included sustained, inhalation-linked glutamate transients; slower, tonic increases in glutamate; rapidly adapting glutamate signals, biphasic responses consisting of a transient increase followed by a decrease below baseline, and even purely suppressive responses. Simultaneous imaging of glutamate and calcium signals from MT cells in the same glomerulus, using iGluSnFR and the red-shifted calcium sensor jRGECO1a, revealed highly correlated pre- and postsynaptic signals across these different response types. Qualitatively similar diversity was seen in the dynamics of glutamatergic input to MT cells in the awake mouse. These results reveal a surprising diversity in the dynamics of excitatory input to MT cells, and suggest that the complex spatiotemporal activity patterns thought to play a critical role in coding odor information at this stage may arise largely from feedforward excitatory pathways, as opposed to being an emergent feature of inhibitory networks. These results also highlight the utility of glutamate imaging for dissecting OB circuit organization and function in vivo.

Keywords: olfaction, olfactory bulb, glutamate imaging, calcium imaging, diversity, mitral and tufted cells

INTRODUCTION

The neural activity underlying odor perception is inherently dynamic. In vertebrates, olfactory sensory input arrives at the brain as bursts of activity driven by each inhalation, and patterns of inhalation are actively controlled by an animal as it samples its environment. At the level of the olfactory bulb (OB), olfactory sensory neurons (OSNs) expressing a single type of odorant receptor converge onto discrete glomeruli (Buck and Axel, 1991; Ressler et al., 1994), where they make excitatory, glutamatergic synapses onto an array of targets including local, juxtaglomerular interneurons and the principal OB output neurons, mitral and tufted (MT) cells (Wachowiak and Shipley, 2006). Odorant responses among MT cells display a rich temporal diversity in their patterns of spiking, with diverse sequences of excitation and suppression that occur with respect to a single inhalation of odorant (Shusterman et al., 2011) and across multiple inhalations, or sniffs (Buonviso et al., 2003; Díaz-Quesada et al., 2018). There is strong evidence that olfactory information is represented both by the identity of activated MT cells as well as by their temporal dynamics (Schaefer and Margrie, 2007; Wilson et al., 2017).

Much of the complexity in response patterns of MT cells has been attributed to processing by OB circuits – in particular, inhibitory circuits that target the apical or lateral MT cell dendrites (Schoppa and Urban, 2003; Shao et al., 2012; Geramita and Urban, 2017). Intrinsic properties of MT cells have also been proposed to contribute to diversity in MT cell temporal responses (Padmanabhan and Urban, 2010) to odors. However, excitatory synaptic inputs to MT cells, which occur solely on the MT cell apical tuft in a single glomerulus, may also contribute to generating temporally complex and diverse patterns of MT cell spiking. For example, OSN inputs themselves respond to odorant inhalation with a range of response latencies, and show nonlinear changes in their activation patterns as a function of odorant concentration, sampling time and sampling frequency (Verhagen et al., 2007; Wachowiak and Cohen, 2001; McGann et al., 2005). Additional diversity in excitatory synaptic input to MT cells can arise from external tufted (ET) cells, a glutamatergic juxtaglomerular interneuron that is a major source of excitatory drive to MT cells (Gire et al., 2012). ET cells respond to OSN input with longer-duration spike bursts and are predicted to entrain their bursting to the sniff

rhythm during repeated odor sampling (Hayar, 2004). ET cells constitute a control point by which inhibitory circuits can regulate MT cell excitation by gating ET cell activation (Banerjee et al., 2015; Gire and Schoppa, 2009). Thus, diversity in the strength and dynamics of glutamatergic input to MT cells, in addition to inhibitory inputs, may be a major contributor to the dynamics of MT cell spiking that are thought to be important in encoding odor information. However, the contribution of glutamatergic input dynamics to MT cell odorant response patterns *in vivo* remains poorly understood.

Here, to characterize the dynamics of glutamatergic input to MT cells, we imaged odorant-evoked and inhalation-linked glutamate signals in glomeruli of the mouse OB using the genetically-encoded glutamate sensor iGluSnFR and its second-generation variants (Marvin et al., 2013; Marvin et al., 2018), expressed selectively in MT cells. iGluSnFR and the SF-iGluSnFRs reported glutamate signals that were confined to the glomerular neuropil and MT cell lateral dendrites, where MT cells release glutamate. Glomerular glutamate transients were tightly coupled to inhalation and reported inhalation-linked dynamics with high signal-to-noise ratio and a higher temporal fidelity than calcium-sensitive reporters, allowing monitoring of glutamatergic signaling across the dorsal OB on a single-trial basis and in the awake mouse. We also directly compared pre- and postsynaptic excitation of MT cells using simultaneous, dual-color imaging of glutamate and calcium signals from MT cells in the same glomerulus. Overall, we observed a surprising diversity in the temporal dynamics of glutamatergic input to MT cells over time scales involving a single inhalation and across multiple inhalations of odorant. We found a surprisingly high correspondence between the dynamics of glutamatergic input and of MT cell output. Our results reveal remarkable diversity in the dynamics of excitatory input to MT cells and suggest that the complex spatiotemporal activity patterns thought to play a critical role in coding odor information at this stage may arise largely from feedforward excitatory pathways. Our results also highlight the utility of glutamate imaging for dissecting OB circuit organization and function in vivo.

METHODS AND MATERIALS

Animals

Experiments were performed on both male and female transgenic mice expressing Cre recombinase (Cre) in defined neural populations with single or dual viral expression of the optical indicator of interest. Mouse strains used were: PCdh21-Cre (Tg(Pcdh21-cre)BYoko) (Nagai et al., 2005), MMRRC Stock #030952-UCD; and Tbet-Cre (Tg(Tbx21-cre)1Dlc) (Haddad et al., 2013; Grobman et al., 2018), Jax Stock # 024507. Mice ranged from 3-8 months in age. Mice were housed up to 4/cage and kept on a 12/12 h light/dark cycle with food and water available *ad libitum*. All procedures were carried out following the National Institutes of Health Guide for the Care and Use of Laboratory Animals and were approved by the University of Utah Institutional Animal Care and Use Committee.

Viral vector expression

Viral vectors driving Cre-dependent expression of iGluSnFR and jRGECO1a (Marvin et al., 2013; Chen et al., 2013; Dana et al., 2016) were obtained from the University of Pennsylvania Vector Core (AAV1 or 5 serotype). SF-iGluSnFR variants were obtained from either HHMI Janelia Campus (A148V & A184S) or Addgene Vector Cores (S72A) (Marvin et al., 2018). All vectors drove expression of each indicator under a human Synapsin (hSyn) promoter in a Cre-dependent manner. Each vector was injected into either the mitral cell layer (MCL) or the deep external plexiform layer (EPL) of the olfactory bulb (OB). For injection, mice were anesthetized with isoflurane (0.5-3%), placed in a stereotaxic headholder and a circular craniotomy was made over the injection site. Injections in the dorsal olfactory bulb were performed using glass pipettes with a diameter of 0.015 mm at the tip, and lowered to a depth of 350-400 μm (in Pcdh21-Cre mice) or 250-300 μm (in Tbet-Cre). For coinjection of jRGECO1a and iGluSnFR, both viruses were diluted 1:10 and injected in separate pipettes within the same craniotomy. After the initial injection, mice were given carprofen (Rimadyl, S.C., 5 mg/kg; Pfizer) as an analgesic and enrofloxacin (Baytril, I.M., 3 mg/kg; Bayer), as an antibiotic immediately before and 24 hours after surgery. Mice were singly housed after

surgery on ventilated racks and used 21-35 days after virus injection for iGluSnFR or SF-iGluSnFR imaging and 21-28 days for SF-iGluSnFR/jRGECO1a imaging.

In vivo two photon imaging

For anesthetized imaging experiments, mice were initially anesthetized with pentobarbital (50 - 90 mg/kg) then maintained under isoflurane (0.5 – 1% in O_2) for data collection. Recordings began 2-3 hours after the start of the preparation. Body temperature and heart rate were maintained at 37 ºC and ~ 400 beats per minute. Mice were double tracheotomized and isoflurane was delivered directly to the lungs via the tracheotomy tube without contaminating the nasal cavity (Eiting and Wachowiak, 2018). Animals were secured through an omega headbar affixed to the skull, then placed on a custom head-mount device and fastened into place as described in previous publications (Wachowiak and Cohen, 2001; Bozza et al., 2004; Spors et al., 2006). Two-photon imaging occurred after thinning and removal of the bone and dura overlying the dorsal olfactory bulb.

Imaging was carried out with a two-photon microscope (MOM; Sutter Instruments) coupled to a pulsed Ti:Sapphire laser (Mai Tai HP; Spectra-Physics, or Chameleon Ultra; Coherent) at 920-940 nm and controlled by either Scanimage 3.9, 5.1 (Pologruto et al., 2003) or Scanbox Yeti 4.0. In these experiments, imaging was performed through a 16X 0.8 N.A. (Nikon) objective and emitted light was collected by multialkali photomultiplier tubes (Hamamatsu R6357, GaAsP H7422). Fluorescence images were acquired at 15.16/15.5 Hz (resonance scanning) for glomerular level imaging with Scanimage or Scanbox instruments respectively. For S72A imaging, bidirectional scanning at 30Hz was utilized to capture faster responses. For dual-color imaging, simultaneous excitation of both fluorophores occurred through a 940nm (Mai Tai HP; Spectra Physics) and 1070nm (Fidelity-2 Ultrafast; Coherent) laser. Dual-color emission was collected through two filters optimized for eGFP (LP 520/65) and TxRed (LP 610/75).

Odorant stimulation

For most experiments, odorants were presented as dilutions from saturated vapor (s.v.) in cleaned, desiccated air using a custom olfactometer under computer control, as described previously (Bozza et al., 2004; Verhagen et al., 2007). Odorants were presented across durations ranging from 2-8 seconds. Filtered, Ultra Zero air was passed across the nostrils in between trials to avoid contribution from extraneous odorants in the environment. All odorants were 95 -99% purity from Sigma (St. Louis, MO) and stored under nitrogen. Odorants were pre-diluted in solvent (mineral oil or MCT oil) to allow for lower final concentrations and then diluted to concentrations ranging from .3% to 3% saturated vapor (s.v). A blank vial consisting of mineral or MCT oil was used as a control. Odorants used with this design included: 2-hexanone, ethyl butyrate, methyl valerate, ethyl tiglate, methyl benzoate, vinyl butyrate, 2-methyl pentanal, trans-2-methyl-2-butenal, menthone, isobutylthiazole, and were either diluted 1:25 or 1:10 respectfully, unless otherwise stated. For experiments testing a larger number of odorants (e.g., Figures 3 and 5, 23 odorants), we used our recently published olfactometer design (Burton et al., 2019). For this preparation, 20μL of each odorant was pipetted in 12 separate mixer tips per odor bank and all tips were oriented in order to ensure proper flow into eductor nozzle and optimally mix within the carrier stream (Burton et al., 2019). The carrier stream maintained a constant 5L/min flow rate, and each solenoid valve for individual odorants was actuated at 30 psi. The olfactometer was placed approximately 8 cm away from the nose.

Analysis of Temporal Dynamics

Image analysis was performed through custom scripts written in MATLAB (Mathworks). For figure display, odor response maps were displayed using ΔF values rather than ΔF/F to minimize noise from nonfluorescence regions. In all quantitative analysis ΔF/F was calculated as

$$\frac{\Delta f}{f} = \frac{f - fo}{fo}$$

Where f is equal to the 95% of the maximum response during the odorant onset and fo is the mean of the baseline response 1-2 sec prior to odorant onset. Activity maps were scaled as indicated in the figure and were kept to their original resolution (512 x 512) and smoothed using a Gaussian kernel with a SD of 1 pixel.

For time-series analysis, regions of interest (ROIs) were initially chosen based on the mean fluorescence image of iGluSnFR expression in the glomerular neuropil and were further refined based on odorant response maps. All ROIs that were excited or suppressed by the “blank” (control) odor were excluded from analysis. For analysis of odorant-evoked dynamics over several seconds, responses to 3 - 8 presentations of odorant were averaged before analysis.

For analysis of inhalation-linked dynamics, inhalation-triggered (ITA) responses were generated by averaging each inhalation (delivered at 0.25 Hz) over a 70 sec odorant presentation (17 inhalations in total). Onset latency was calculated as the first time point in which the following 4 frames of an ITA trace were above the threshold for a significant excitatory response, which we defined as 4 SD above the fluorescence signal from a 1 s pre-stimulus window. To calculate decay time-constants (Figure 1), a single exponential was fitted from the peak of the ITA trace and extending to the end of the trace. Peak response amplitudes and time-to-peak values were calculated from filtered ITAs as the maximum of the response. From this trace, response duration (full-width at half-maximum) was calculated as the time from 50% of peak response on the rising slope of the signal to 50% of peak on the decaying slope of the signal.

Decorrelation Analysis

Time series data for two experiments spanning five total fields of view was averaged across 3-trials per odorant, low-pass filtered at 2 Hz, z-score normalized using 2 secs prior to odor stimulation as baseline, and grouped into five time bins, representing 0.386 seconds per bin. The first 10 time bins (150 msec) were omitted to account for delays in odorant onset. Calcium signals for all ROIs (significant and non-significant) were averaged for every odorant within each of the five time bins. Pearson’s correlation coefficient (*r*) was calculated between the population of ROIs in a field of view within the first time bin against the ROIs within every subsequent bin, producing

“decorrelation” (i.e. correlation to early) values. We also calculated an overall correlation time series by computing the mean and SE for all 115 ROIs together.

Concentration Analysis

Significant responses were sorted by categorizing each glomerulus-odor pair at the lowest odor concentration. We then calculated T2-T1/Tmax (Fig. 4) as the difference in amplitude between the peak ΔF following the first (T1) and the second-to-last (T2) sniff divided by the maximum of the overall trace during the 4 second odor presentation. Coherence relative to the 2Hz artificial inhalation was defined as:

$$C_{xy}(f) = \frac{|P_{xy}(f)|^2}{P_{xx}(f)P_{yy}(f)}.$$

Where $P_{xx}(f)$ and $P_{yy}(f)$ is the magnitude-squared coherence of the power spectral densities (taken from 2Hz inhalation rates) and the cross power spectral density, $P_{xy}(f)$ of x and y.

Single and Two-Color Novel Olfactometer Analysis

Response patterns across a 24-odorant panel (i.e., Figure 3, Figure 5) were scored as excitatory, suppressive or biphasic based on deviation from the pre-stimulation baseline using the following criteria. For single color imaging, odorant responses were averaged across 3 odorant presentations (trials); and for two-color imaging data used 4-trial averages. To identify and categorize responses as having significant excitatory or suppressive components, average responses were low-pass Gaussian filtered at 2 Hz (to test for excitatory responses) or 0.5 Hz (for suppressive responses) and z-score standardized using a baseline from 2 to 0.5 sec prior to odorant onset, with z defined as the SD of the baseline period concatenated for all 24 odorant responses. Peak excitation was measured as 95% of the maximum signal during the 3- or 4-second odorant presentation; suppressive responses were measured as the 25th percentile of all values in a time-window from odorant onset to 500 msec after odorant offset, to account for the slower dynamics of suppression and the low-pass filtering of the signal. We then used a conservative criterion for significance of z = 7 (7 SD) for

defining significant excitatory or suppressive responses. This cutoff was chosen to yield a false positive rate of approximately 1% (based on visual inspection of traces).

To correlate iGluSnFR and jRGECo1a signals in the dual-color imaging experiments, Pearson's correlation coefficients (*r*) were calculated from each average odor response, over a time-window from 2 sec before to 10 sec after odor presentation.

Histology

Following an experiment, mice were euthanized and transcardially perfused with 1x phosphate buffered saline (PBS) and 4% paraformaldehyde (PFA). After decapitation, the entire brain with the olfactory bulbs was excised and placed into a solution of equal parts 4% PFA and 1x PBS overnight. Post-experimental tissue was cut coronally into 200μm thick sections on a vibratome (Leica) to verify expression of the indicator across the olfactory bulb.

Awake Imaging

Adult Tbet-cre mice for awake experiments were surgically implanted with an aluminum headbar centered over lambda, as described previously (Burton et al., 2019). Next, a craniotomy over the left OB was performed, and 500-750nL of AAV2.5.hSyn.SF-iGluSnFR.A184V.WPRE was injected 250μm deep into the bulb at a rate of 100μL/min using a glass pipette. The injection pipette was held in place for 10 minutes post injection. During this time, the surface of the bulb was kept wet with sterile saline. After removing the injection needle, a double coverslip was installed over the craniotomized bulb, and affixed into place using dental cement (Teets). Agarose (2%, low-melting point) was used to fill in the interstitial spaces. The double coverslip was created as a combination of two pieces of custom-cut glass (Matsunami Glass, Bellingham, WA), glued together with UV-cured glass glue (Norland Optical Adhesive, No. 61). The inner glass was a round, 1.5 mm-diameter piece, affixed to a larger, 2.7 or 3.0 mm-diameter piece. This larger, outer piece rested on the margins of the craniotomy, while the inner piece formed a tight seal with the dura. Animals were allowed to recover for a minimum of two days post-surgery.

Mice were acclimated to the imaging rig for one 30-minute session the day prior to imaging. Imaging sessions lasted from 30-60 minutes per day, over the course of several days. The behavior and imaging apparatus has been described previously (Economo et al., 2016; Burton et al., 2019). Briefly, mice were affixed in place over a styrofoam ball, floating on an air cushion. Mice were naïve to the odors at their first imaging session. Imaging was carried out on glomerular neuropil under 2-photon microscopy at 940 nm wavelength (Scanbox Yeti 4.0). Odors were presented as in our anesthetized experiments. Odor pulse duration was 4 seconds, followed by 20 second inter-trial intervals. Respiration (sniff) signals were collected by placing a highly sensitive pressure probe (First Sensor, AG, Berlin, Germany, part no. FBAM200DU) in front of the animal's right nostril (Jordan et al., 2018). At least 8 trials per odorant per session were collected. Occasionally, a brief (100 msec) air puff, directed at the lower back of the animal, was used to stimulate high frequency sniffing.

RESULTS

Imaging glutamate signaling across mitral/tufted cell dendrites

We first performed a basic characterization of sensory-evoked glutamate signals reported by iGluSnFR (Marvin et al., 2013) and its second-generation variants, which have a range of affinities for glutamate (Marvin et al., 2018). iGluSnFR expression was targeted to MT cells using Cre-dependent viral vectors injected into the olfactory bulb of Pcd-Cre or Tbet-Cre transgenic mice. All iGluSnFR variants showed expression that appeared enriched on the membrane surface (Figure 1A, bottom) and which spanned all cellular compartments (Figure 1A, top). When imaged in vivo with two-photon laser scanning microscopy, resting fluorescence showed clearly-delineated glomeruli, as expected from expression across MT cell apical dendrites (Figure 1B).

We have previously shown, using the first-generation iGluSnFR, that each inhalation of odorant drives a transient of glutamate release onto juxtaglomerular interneuron processes in the glomerular neuropil (Brunert et al., 2016). We observed similar glutamate signals with iGluSnFRs expressed in MT cells (Figure 1B, top). A striking feature of these signals, however, was the considerable diversity in the dynamics of odorant- and inhalation-evoked glutamate transients, with different

glomeruli showing glutamate transients with varying onset latencies and durations, and with distinct changes in the glutamate signal evoked by successive inhalations across a longer odorant presentation (Figure 1B, bottom). Before investigating this diversity further, we more fully characterized sensory-evoked glutamate signals as reported by iGluSnFR expressed across different MT cell compartments. We also characterized signals reported by the three second-generation SF-iGluSnFR variants that are reported to have higher, medium and lower affinities for glutamate: A184S (reported K_d, 7 μM), A184V (K_d, 40 μM) and S72A (K_d, 200 μM) (Marvin et al., 2018).

The different SF-iGluSnFR variants showed response amplitudes to odorant inhalation that increased with affinity of the variant (Figure 1C, bottom left), with maximal response amplitudes (90th percentile of all glomerulus-odor pairs: S72A: 23%, A184V: 74%, and A184S: 104% ΔF/F). We next compared inhalation-linked dynamics of glutamate signals by generating 'inhalation-triggered' average responses (ITAs) from multiple inhalations at low (0.25 - 0.5 Hz) frequency, as we have done previously (Díaz-Quesada et al., 2018; Short and Wachowiak, 2019) (see Methods). We compared ITAs generated across multiple glomerulus-odor pairs using the three second-generation SF variants. Each variant tracked single inhalation responses with high fidelity**.** The shortest decay time following each inhalation (25th percentile across all glomerulus-odor pairs; S72A: n=16, A184V: n=91, A184S: n=370) varied according to SF-iGluSnFR affinity, ranging from 117 msec for S72A, 162 msec for A184V and 297 msec for A184S (Figure 1C). However, across all glomerulus-odor pairs, decay times varied for different glomerulus-odor combinations and the range of decay times overlapped across the three variants (Figure 1C, bottom right). In some cases, inhalation-linked response transients were more complex than a simple fast rise and exponential decay, for example including a 'shoulder' component resulting in a longer-duration glutamate signal (not shown). Overall these results suggest, at least for the medium and high-affinity SF-iGluSnFRs, that variation in the dynamics of the iGluSnFR signal imaged from MT cell apical tufts is largely indicative of the variable dynamics of glutamate signaling in the glomerulus, as opposed to intrinsic kinetic differences of the reporter.

The apical dendritic tuft within the glomerulus is the only reported site of glutamatergic input onto MT cells (Schoppa and Urban, 2003); however, MT cells are

known to also release glutamate from dendrodendritic synapses on their apical tuft and lateral dendrites (Isaacson, 1999; Isaacson and Strowbridge, 1998). To assess glutamate signaling across the MT cell dendritic field, we used the high-affinity A184S variant and imaged at high zoom from the apical tuft, primary dendrite, and lateral dendrites. In the superficial OB, odorant-evoked glutamate signals were restricted to MT cell apical tufts throughout the neuropil of responsive glomeruli (Figure 1D). While SF-iGluSnFR expression was apparent along the length of the MT cell apical dendrite as it entered a glomerulus, evoked glutamate signals were confined to the dendritic tuft within the glomerulus (Figure 1D, 1E). Likewise, glutamate signals were absent from MT cell somata (Figure 1D, 1E).

Using A184S to image from the external plexiform layer (EPL), odorant stimulation elicited smaller-magnitude glutamate signals along MT cell lateral dendrites, with different odorants evoking signals in different subsets of lateral dendrites (Figure 1F). Since MT cells are not thought to receive glutamatergic input via their lateral dendrites (Margrie et al., 2001), we interpret these signals as reflecting glutamate release from the same cells on which the reporter is expressed. Glutamate signals appeared continuous along the length of a lateral dendrite, although we did not attempt to image at a high enough zoom to resolve potentially localized release sites, and spines are not present on MT cell lateral dendrites. Some dendrites appeared to show weak odorant-evoked fluorescence decreases, suggesting a decrease in ongoing release associated with odorant stimulation (Figure 1F, ROIs 3&4, right). Taken together, these data indicate that SF-iGluSnFRs report glutamatergic input onto MT cell apical dendrites with high fidelity, and can also report glutamate release from MT cell lateral dendrites at a substantial distance from the MT soma.

Diverse temporal patterns of glutamatergic signaling across multiple time scales

The timing of odorant- and inhalation-evoked MT cell spiking varies across MT cells and across odorants, and has long been hypothesized to play a role in coding odor information (Shusterman et al., 2011; Díaz-Quesada et al., 2018; Carey and Wachowiak, 2011; Wachowiak, 2011). To assess the degree to which such variability is present at the level of glutamatergic input onto MT cells, we analyzed inhalation-linked

onset dynamics of the iGluSnFR signal for all glomerulus-odor pairs. We first analyzed inhalation-triggered average response waveforms (ITAs), derived from low-frequency (0.25 Hz) inhalations imaged with SF-iGluSnFR.A184S and A184V (Short and Wachowiak, 2019; Díaz-Quesada et al., 2018). While odorants evoked distinct combinatorial patterns of glutamate signals across glomeruli, as expected (Figure 2A), they also elicited inhalation-triggered dynamics that varied substantially across glomeruli and odorants (Figure 2B). Glomeruli activated by the same odorant could show ITA waveforms with different onset latencies, rise-times, and durations, and the same glomerulus could show distinct ITA dynamics for different odorants (Figure 2B). Across all glomeruli imaged with A184S (n = 431 G-O Pairs, 5 mice), ITA onset latencies ($10^{th}/90^{th}$ percentiles) ranged from 113-253 msec, and time to peak ranged from 300 msec–533 msec (Figure 2C), with durations ranging from 360 msec–867 msec (Figure 2C). Notably, inhalation also could elicit fluorescence decreases in a glomerulus, suggesting a phasic decrease in ongoing glutamate release (Figure 2B, ROI 6, although this was rare). Responses using the A184V variant were similar, with onset latencies ranging from 153-313 msec. Response durations of A184V ITA responses also showed a wide range of values, from and 260 msec – 1.1 sec as well as time to peak responses ranging from 313 msec -727 msec (n = 113 G-O Pairs, 3 mice, $10^{th}/90^{th}$ percentiles). Thus, the dynamics of glutamatergic input onto MT cells spans a potentially wide range and can vary substantially depending on both glomerular and odorant identity.

We have previously reported similar variability in inhalation-linked dynamics of OSNs themselves, as reflected in calcium signals in their presynaptic terminals in the glomerulus (Short and Wachowiak, 2019; Spors et al., 2006). We thus compared the variability seen in the glutamate ITA with that seen in the recently published data from OSNs expressing the genetically-encoded reporter GCaMP6f (Short and Wachowiak, 2019) (Figure 2D). ITA onset latencies for OSN inputs to glomeruli were, as a population, longer than those for iGluSnFR (mean ± SD: OSN-GCaMP: 0.268±0.1 sec, MTC-A184S: 0.188±0.06 sec), reflecting the slower response time of GCaMP6f compared to iGluSnFR. However, the variability in ITA latencies was similar for these two signals, with overlapping onset latencies across the two populations after

subtracting the median latency for each (10th/90th percentiles: OSN-GCaMP6f: -0.08/0.13 sec, MTC-A184S: -0.07/0.067 sec). These results suggest that variability in the onset times of glutamate transients onto MT cell after each inhalation largely reflect variability in the timing of spike bursts arriving at OSN presynaptic terminals.

Diversity of glutamatergic signaling across multiple sniffs.

To more fully investigate the temporal diversity in patterns of glutamate signaling onto MT cells, we imaged responses across the dorsal OB to 23 odorants, using our recently published olfactometer design (Burton et al., 2019). Odorants were presented for 2 seconds each using an artificial inhalation rate of 3 Hz, and delivered at relatively low concentrations across most odorants (~0.5% s.v. of odorants diluted at liquid concentrations of 1:500, 1:100, 1:10, or neat) such that each odorant evoked relatively sparse responses across the field of imaged glomeruli (Figure 3A), with 16.8% of all glomerulus-odor pairs (588/3496; 5 fields of view from 2 mice) showing responses that were significant according to conservative criteria for an odorant-evoked change in iGluSnFR fluorescence (see Methods) (Figure 3D).

We observed considerable diversity in the temporal patterns of odorant-evoked glutamate signals (Figure 3B). Patterns were robust, occurring consistently over repeated presentations (not shown). The most common response pattern consisted of a simple increase that was sustained over the 2-second presentation and returned rapidly to baseline at the end of presentation (Figure 3C, e.g., Isopropyl tiglate). However, other excitatory response patterns were common, including transient increases occurring immediately after odorant onset and not following any subsequent sniff, prolonged increases that returned slowly to baseline after odorant offset, and slow rises in glutamate over the 2-second presentation (Figure 3C, e.g., Hexanoic acid). Notably, odorants could also evoke responses with a strong suppressive component; these included biphasic (excitatory and suppressed) responses consisting of a brief increase in glutamate followed by a sustained decrease below baseline (seen in 3.4% (20/588) of significant responses) as well as responses consisting solely of fluorescence decreases (seen in 7.1% (42/588) of significant responses) (Figure 3D). Response patterns varied for different glomeruli activated by the same odorant and for responses of the same

glomerulus to different odorants (Figure 3C, yellow trace, ROI 3), indicating that response patterns were neither a function of iGluSnFR expression levels in a particular glomerulus nor a function of any particular odorant.

One consequence of this diversity was that the relative magnitude of glutamatergic signaling in different glomeruli—and thus the glomerular representation of an odorant—could vary over the 2-second odor presentation. To quantify this, we correlated patterns of glutamate signals across the imaged glomeruli in a field of view at each 386 msec time bin, starting 150 ms after odorant onset. Among all glomerulus-odor pairs, there was a substantial decrease in correlation beginning in the second bin (mean r ± SEM, time bin 2: 0.55 ± 0.32) to the last bin (time bin 5: 0.43 ± 0.38), although the degree of decorrelation varied greatly across glomerulus-odor pairs, with correlation coefficients at the end of the 2 sec presentation ranging from -0.54 to 0.98 (Figure 3E). For example, as seen in Figure 3C (insets), responses to some odorants decorrelated substantially after the initial response (Figure 3C, e.g., hexanoic acid, heptanal) while responses to other odorants remained consistent (Figure 3C, e.g., isopropyl tiglate). This decorrelation is qualitatively similar to that observed in patterns of MT cell spiking over repeated samples of odorant (Díaz-Quesada et al., 2018; Bathellier et al., 2008), suggesting that time-dependent decorrelation can arise at the level of glutamatergic input to MT cell.

Odorant concentration systematically alters the dynamics of glomerular glutamate signals

Distinct temporal patterns of glutamatergic signaling could be determined by the strength of odorant stimulation for a given glomerulus, relative to the dynamic range of that glomerulus for the odorant. Such temporal patterns could be achieved by inducing rapid adaptation or sustained responses (Lecoq et al., 2009; Matsumoto et al., 2009). To address this, we investigated the effect of odorant concentration by presenting a smaller number of odorants (3 – 5 per experiment, n = 4 mice) at 3 concentrations spanning a 10-fold range, using first-generation iGluSnFR (Marvin et al., 2013). Changing concentration could dramatically alter the dynamics of the glutamate response over the time of a 4-second odorant presentation (Figure 4A). In many

glomerulus-odor pairs, odorants evoked consistent inhalation-driven transients throughout odorant presentation at the lowest (1x) concentration, which changed to highly adapting responses at higher concentrations, with a strong reduction in glutamate levels from the beginning to end of presentation (Figure 4A, e.g., methyl valerate, ethyl tiglate). In other glomeruli (even for the same odorants), increasing concentration appeared to recruit glutamate signals with repeated inhalations over the course of the presentation; this often included an increase in the tonic component of the glutamate signal (Figure 4A). Other glomerulus-odor pairs showed little adaptation and little effect of concentration (Figure 4A, e.g., 2-hexanone).

To quantify these changes along a particular dimension of response pattern, we calculated T2-T1/Tmax (Figure 4B, See Methods) across 189 glomerulus-odor pairs. With this measure, negative values indicate adaptation while positive values indicate facilitation. At all concentrations, there was a high degree of variability in changes in glutamate signal over time (Figure 4B), although across the population, increasing concentrations trended towards adaptation (n=189 G-O pairs, mean±SD, one sample t-test, 1x: -0.19 ± 0.35, $p = 2. x10^{-12}$, 3x: -0.14 ± 0.40, $p = 5 \times 10^{-6}$, 10x : -0.26 ± 0.44, $p = 8 \times 10^{-14}$). There was a very slight but significant increase in adaptation (or loss of facilitation) as concentrations increased from 1x to 10x (p=0.044, paired t-test), although the variance of effect across the population remained high.

A second effect of increasing odorant concentration was a reduction in the degree to which glutamate signaling was modulated by each inhalation, with many glomeruli showing a loss of inhalation-linked transients, being replaced by a tonic glutamate signal (Figure 4D, 4E). We quantified this effect by measuring the coherence of the iGluSnFR signal relative to a simulated 2Hz inhalation pulse (see Methods). Across all glomerulus-odorant pairs, coherence with inhalation decreased with increasing concentration (Figure 4C) (mean ± SD, 1x: 0.86 ± 0.16, 3x: 0.75 ± 0.28, 10x: 0.56 ± 0.32). Notably, however, this effect varied depending on the odorant used ($F_{1,188} = 4$, p = 0.004, one-way ANOVA) (Figure 4D), with glomeruli responsive to the ketone 2-hexanone showing little loss of inhalation-linked coherence as concentration increased while glomeruli responsive to the other tested odorants (3 esters and one tiglate) showed a loss of coherence (Figure 4C). These odorant-specific differences may reflect

differences in the kinetics of odorant sorption or clearance from the nasal epithelium, although further experiments are necessary to resolve this question. Overall, these results indicate that odorant concentration has systematic impacts on the dynamics of glutamatergic signaling onto MT cells, with a general (but slight) increase in adaptation and a substantial decrease in inhalation coupling as odorant concentration increases.

Correspondence between glutamatergic dynamics and postsynaptic activity in MT cell

While glutamatergic signaling in the glomerulus is the sole source of excitatory input to MT cells, multiple inhibitory circuits are thought to shape patterns of MT cell excitation via feedforward, recurrent and lateral inhibition (Burton, 2017). Because MT cell spikes back-propagate along the MT cell apical dendrite and invade the apical tuft (Djurisic et al., 2008), calcium imaging from the tuft provides a good proxy for patterns of MT cell spike output from each glomerulus (Economo et al., 2016; Charpak et al., 2001). Thus, we reasoned that comparing glutamate signals onto MT cells with calcium signals in MT cell apical dendrites of the same glomerulus would provide insights into the relative contributions of excitatory versus inhibitory inputs to MT cell response patterns.

To achieve this, we simultaneously imaged glutamate and calcium signals in MT cells of the same glomeruli by co-expressing SF-iGluSnFR.A184S and the red calcium reporter jRGECO1a (Dana et al., 2016) in MT cells (see Methods) (Figure 5A). Post-experimental histology confirmed that both indicators expressed well in the cytoplasm and membrane of MT cells (Figure 5A) We first characterized responses to a few odorants per preparation, comparing response dynamics at 1Hz inhalation rates and comparing the distribution of signals within a glomerulus. As expected, jRGECO1a signals were apparent both in an activated glomerulus as well as in the apical dendrites of the MT cell innervating it, while iGluSnFR signals did not extend beyond the glomerulus boundaries (Figure 5B). At low inhalation frequency (0.25 Hz), odorant-evoked ITA waveforms were similar for iGluSnFR and jRGECO, with jRGECO signals lagging iGluSnFR signals, as expected given the slower on- and off kinetics for jRGECO (Dana et al., 2016) (not shown). At inhalation frequencies of greater than 1 Hz, however, jRGECO signals showed less modulation by each inhalation (e.g., Figure 5E).

To compare the diversity of response patterns seen in these two signals, we performed dual-color imaging using the same 24 odorant panel as for the single-color imaging (in 5 fields of view from 3 mice) but using 4-second rather than 2-second presentations (Figure 5C-E). We saw the same diverse range of response patterns in these experiments as in the single-color experiments, including sustained, rapidly adapting, facilitating and suppressive components (Figure 5D, 5E). Overall, there was a surprising degree of correspondence in response patterns of the two signals (Figure 5D, 5E). Rare cases of lack of correspondence between glutamate and calcium signals are shown for glomerulus 2 in Figure 5D, where 4 of the 11 odorants elicit suppression in the jRGECO1a signal; in three of these cases, iGluSnFR elicits a biphasic response consisting of a brief initial increase followed by a decrease in glutamate; the initial excitatory transient is not apparent in the calcium signal.

We quantified the correspondence between iGluSnFR and jRGECO response patterns first by computing correlation coefficients between the two signals for each glomerulus-odor pair tested (see Methods). In general, correlation coefficients were high: for all glomerulus-odor pairs showing a significant response (defined conservatively as ± 7 SD above pre-odor noise) in at least one of the signals (n = 526 G-O Pairs, 3 mice), the mean correlation (Pearson's r) was 0.80 ± 0.18 (SD). Correlations across all glomerulus-odor pairs (n = 3,788 pairs from 3 mice), including those that did not meet our conservative criterion for a significant response, were variable but also relatively high, with a mean correlation of $r = 0.45 \pm 0.26$. We also examined the concordance between excitatory response types reflected in the two signals. There was strong concordance in glomeruli showing simple excitatory responses as measured with iGluSnFR and jRGECO: 70% (244/350) of glomerulus-odor pairs with an excitatory iGluSnFR signal also showed a significant jRGECO response, and 79% (244/309) of glomeruli with significant jRGECO increases showed excitatory iGluSnFR signals.

Comparing concordance (or lack thereof) between pre- and postsynaptic signals among suppressive responses is especially informative, as this could reveal differential impacts of inhibitory inputs to MT cells, for example by feedforward or lateral inhibition. Such an analysis was difficult: while responses with suppressive components were

clearly apparent even on single trials (i.e., Figure 5D), their small amplitude and the relatively few repeat trials given (3 - 4 per odorant) resulted in a likely underestimation of their prevalence based on the strict significance criteria we used. Nonetheless, jRGECO responses with suppressive components were detected 3 - 4 times more frequently than iGluSnFR responses, being present in 1.5% (55/3788) versus 0.4% (15/3788) of all glomerulus-odor pairs, and 15% versus 4% of all significant responses. Notably, suppressive jRGECO responses were essentially never seen along with excitatory iGluSnFR responses (detected in 1 of 55 cases, which is approaching the false positive rate). Thus, while preliminary, these results are consistent with interglomerular inhibition suppressing MT cell spiking in a small fraction of glomeruli (Economo et al., 2016; Banerjee et al., 2015), but are inconsistent with feedforward inhibition suppressing MT cell spiking in glomeruli receiving weak excitatory input (Cleland and Linster, 2012).

Glomerular glutamate signaling shows diverse temporal dynamics in awake mice

Finally, to assess diversity in glutamate signaling onto MT cell during natural odor sampling, we imaged iGluSnFR signals from dorsal glomeruli in awake, head-fixed mice (Figure 6). Respiration frequency for most trials ranged from 3 – 6 Hz (mean ± SD, 4.5 ± 1.8 Hz), with occasional pauses and bouts of high-frequency sniffing.

Qualitatively, glutamate transients seen in awake mice showed the same diversity of response dynamics as those seen with artificial inhalation. First, there was variability in the degree of coupling of iGluSnFR signals to respiration: for the majority of responsive glomeruli, each inhalation at the 'resting' frequencies of 3 – 6 Hz elicited a clear glutamate transient (Figure 6A, 6B). However, for other glomerulus-odorant pairs, glutamate signals were not clearly modulated by respiration but instead consisted largely of a tonic glutamate increase (not shown). Second, for glomeruli where glutamate signals were modulated by inhalation, the latency of the glutamate transient varied across glomeruli and odorants. Latency differences were consistent across repeated inhalations of odorant (Figure 6B). We measured inhalation-linked latencies for glomerulus-odorant pairs by constructing ITA waveforms as done with artificial inhalation, but using the external flow sensor to determine inhalation timing. Because of

the higher frequency of inhalations, ITA waveforms generated from these data resembled a sine wave (Figure 6B, lower left). As seen with artificial inhalation, glomeruli activated by some odorants showed clearly distinct ITA latencies; for example, glomeruli in the same FOV activated by ethyl butyrate showed latencies ranging from 100 – 160 msec (Figure 6B, lower right); however, for other odorants (not shown) there was little variation in ITA latencies across all activated glomeruli, suggesting that odorant inhalation drives near-synchronous bursts of glutamatergic input to MT cells in different glomeruli.

Glutamate signals also showed diverse odorant responses over multiple inhalations. As with artificial inhalation, the evolution of responses over several seconds of odorant presentation included slow increases in tonic glutamate and adaptation of inhalation-linked and tonic glutamate signals. We also observed concentration-dependent changes in glutamate dynamics, with increasing odorant concentrations leading to stronger adaptation of glutamate signal for strongly-responsive glomeruli and recruitment of slowly-increasing responses in weakly-responsive glomeruli (Figure 6C). Overall, these data indicate that the diversity in dynamics of glutamatergic inputs to MT cells that we observed with artificial inhalation in anesthetized mice is also present in awake, actively-sniffing animals.

DISCUSSION

Temporally complex patterns of excitation and inhibition are a hallmark feature of odor-evoked activity among principal cells (i.e., MT cells) of the OB. Features of this complexity include odorant- and glomerulus-specific latency differences relative to inhalation, suppressive response components, nonlinear concentration dependence, and decorrelation of glomerular odor ‘representations’ over multiple samples. Each of these features has been hypothesized to play an important role in coding olfactory information (Bathellier et al., 2008; Spors et al., 2006; Burton et al., 2012; Economo et al., 2016) and most have been attributed to emergent features of excitatory and inhibitory circuit interactions. Here, by directly imaging glutamate signaling onto MT cell dendrites of OB glomeruli, we observed a striking degree of temporal complexity in this signaling, which parallels that characterized at the level of MT cell spiking, both on the

time-scale of a single inhalation or respiratory cycle and over a slower time scale involving repeated samples of odorant. Similarities in the diversity of glutamate signaling and that of MT activity went beyond qualitative or statistical similarities: by simultaneously imaging both presynaptic glutamate and postsynaptic calcium from MT cells in the same glomerulus, we found a high correspondence in diverse response patterns on both short and longer time scales. These results suggest a model of OB circuit function in which diverse dynamics of sensory input combined with feedforward excitatory circuits can account for much of the diversity of MT cell responses that are thought to mediate identity- and timing-based odor codes in vivo.

Circuit mechanisms of diversity in glutamate signaling

A major source of diversity in excitatory inputs to MT cells is OSNs themselves. OSN inputs converging on a glomerulus have long been known to respond with different latencies relative to inhalation in a glomerulus- and odor-specific manner (Spors et al., 2006; Short and Wachowiak, 2019; Carey et al., 2009); indeed we observed a close match in the range of response latencies for iGluSnFR signals and those measured from OSN presynaptic terminals by Short & Wachowiak (2019) (e.g., Figure 2D). However, we also saw variation in other aspects of inhalation-linked glutamate dynamics, most notably response duration (e.g., Figure 2B, 2C), with the duration of the inhalation-linked glutamate transients ranging from as short as 200 msec to over 1500 msec depending on the glomerulus-odor pair. Whether this variation reflects different OSN activation dynamics or arises from circuit effects, as addressed below, remains to be determined.

Complex dynamics over a slower time scale may also arise at the level of OSN activation. For example, OSNs may show distinct response patterns over multiple samples of odorant depending on the concentration of the odorant relative to the affinity of responsive OSNs, as well as the duration of the odorant in the nasal cavity. In this scheme, odorants at low relative concentration (near the low end of the sensitivity range for a given glomerulus) may drive enhanced responses as odorant concentration at the nasal epithelium is increased during repeated sampling. At the same time, repeated sampling can lead to reduced responses to odorants at the high end of the sensitivity

range, due to adaptation of OSNs or depression of OSN transmitter release (Murphy et al., 2004). These effects could underlie the nonlinearities in glutamate signal seen over the course of odorant presentation and as a function of odorant concentration. In addition, each of these effects may be amplified or gated by increasing sampling frequency, such as occurs during active sniffing. Interestingly, comparable levels of richness in response kinetics and nonlinearities have been well-characterized in OSNs in Drosophila, where such features can be attributed to odorant receptor identity and which contribute to odor coding capacity (Hallem and Carlson, 2006; Geffen et al., 2009).

A second major source of diverse glutamate signaling onto MT cells is feedforward disynaptic excitation mediated by external tufted (ET) cells, which are thought to be a major source of glutamatergic drive throughout the glomerulus (Hayar et al., 2004; De Saint Jan et al., 2009; Najac et al., 2011). ET cells have been hypothesized to be a primary driver of MT cell excitation (Gire et al., 2012; Vaaga and Westbrook, 2016), although the degree to which ET cells drive MT cell excitation in vivo remains uncertain. ET cell-mediated glutamatergic drive could underlie the longer-duration glutamate transients seen in our data, as well as facilitation of glutamate signals over repeated samples, as ET cells become progressively entrained to the inhalation rhythm (Hayar, 2004). Likewise, gating of ET cell excitation by inhibitory juxtaglomerular circuits may underlie short-duration odorant-evoked glutamate transients or the suppressive components observed in a minority of responses(Liu et al., 2016), (Gire and Schoppa, 2009). Numerous studies have found that inhibitory circuits regulate MT cell excitability through their inhibitory action on ET cells (Whitesell et al., 2013; Murphy et al., 2005; Liu et al., 2016; Banerjee et al., 2015), affecting concentration-response functions and altering the tuning of MT cells to a range of odorants (Banerjee et al., 2015). Ultimately, while the relative contributions of direct OSN inputs versus juxtaglomerular circuits to the dynamics of glutamate signaling onto MT cells is unclear, the use of iGluSnFR as a tool to monitor presynaptic inputs separately from (and simultaneously with) postsynaptic activation provides a powerful approach to dissecting these contributions in vivo.

This all-optical approach to dissecting neural circuits does, however, require

consideration of caveats and technical limitations in interpreting these signals as independent measures of pre- and postsynaptic activity in the glomerular circuit. One concern is that Ca^{2+} signals in the MT cell apical tuft could largely reflect subthreshold synaptic input as opposed to MT cell action potential firing that back-propagates into the tuft, which would of course lead to overestimation of the correspondence between glutamatergic input and MT cell output patterns (since one would directly drive the other). However, several lines of evidence suggest that this is unlikely to be the case. First, previous studies suggest that back-propagating action potentials are the predominant driver of Ca^{2+} signals in the MT cell apical tuft (Charpak et al., 2001; Debarbieux et al., 2003), and over a large number of experiments we have observed a near-perfect correlation among odor-evoked Ca^{2+} signals in the apical tuft, shaft, and soma (see, for example, Figure 5B) (Economo et al., 2016). Second, close inspection of dual-color imaging data reveals numerous cases of iGluSnFR transients that fail to drive Ca^{2+} signals in the same glomerulus, especially when these transients are rapid or small-amplitude (e.g., Figure 5D). We have also observed failure of spontaneous iGluSnFR transients to drive corresponding jRGECO signals (not shown). A second potential concern is that the iGluSnFR signal may reflect glutamate release via dendrodendritic synapses in the MT cell apical tuft (Murphy et al., 2005), (Schoppa and Urban, 2003) and thus not accurately reflect glutamatergic input to MT cells. Dendritic release would also, of course, artificially boost correspondence between the iGluSnFR and jRGECO signals. However, iGluSnFR signals imaged from MT cell lateral dendrites (which we do interpret as reflecting dendritic release) were substantially smaller than those imaged from the apical tuft (see Figure 1E). In addition, we have failed to observe iGluSnFR signals evoked by antidromic stimulation of MT cell axons (n = 2 mice, not shown). Thus, while additional experiments focused on these technical issues will be helpful, we believe that the high correspondence between iGluSnFR and jRGECO signals seen in MT cells largely reflects the strong contribution of feedforward excitatory signaling to the dynamics of MT cell output patterns.

Utility of SF-iGluSnFR for dissection of neural circuits

Glutamate sensors and other genetically encoded transmitter indicators have

emerged as useful tools for the dissection of neural circuits (Marvin et al., 2018; Patriarchi et al., 2018; Sun et al., 2018; Liu et al., 2019). Here, we extend these results to the olfactory system by demonstrating the utility of iGluSnFR and its second-generation variants to robustly report glutamate signaling onto MT cells with high signal-to-noise ratios and high temporal fidelity, and in both anesthetized and awake preparations. Notably, even the lowest-affinity SF-variant, S72A, yielded easily detectable signals which to our knowledge has not thus far yielded signals in response to natural stimuli in cortex. Advantages for glutamate imaging in the OB relative to other brain areas such as cortex may be the high density of glutamatergic synapses in the glomerular neuropil, the high degree of convergence of OSNs activated near-simultaneously within a glomerulus, and the high probability for glutamate release from the OSN presynaptic terminal (Murphy et al., 2004).

Another important advantage of iGluSnFR is its improved kinetics relative to other genetically-encoded reporters such as GCaMPs, an advantage which has been noted in other model systems (Richter et al., 2018). The faster onset and decay times of iGluSnFR are crucial for monitoring neural dynamics in the frequency range of respiration or sniffing in behaving mice, which ranges from approximately 2 – 10 Hz. This advantage was plainly evident in our dual-color imaging experiments, in which jRGECO1a signals showed little modulation of their signal even at 2 Hz artificial inhalation, while iGluSnFR signals imaged in the same trial were strongly modulated (e.g, Figure 5B). In fact, we were able to observe clear glutamate transients from each inhalation in awake, head-fixed mice at sniff frequencies up to and, in some cases, exceeding 5 Hz. As demonstrated by our sniff-triggered average waveforms generated from the awake mouse (e.g., Figure 6B), this improved temporal fidelity will be important in addressing hypotheses about determinants of the relative timing of excitatory inputs to MT cells in different glomeruli and the role of this timing in odor coding (Wilson et al., 2017).

ACKNOWLEDGMENTS

We thank Loren Looger and Jonathan Marvin and the GENIE project from HHMI Janelia Research Campus for sharing SF-iGluSnFR virus. We also thank M. Economo,

D. Brunert and Y. Tsuno for initial characterization of iGluSnFRs, G. Vasquez-Opazo, R. Kummer and J. Ball for technical assistance, and T. Rust for data analysis software. S. Burton, S. Short, I. Youngstrom, provided helpful feedback and discussion. This work was supported by the NINDS T32NAS076067 (to A.K.M) and NIDCD R01DC006441 (to M.W.) and F32DC015389 (to T.P.E).

CONFLICT OF INTEREST

These authors declare no competing financial interests.

CONTRIBUTIONS

A.K.M and M.W. designed research. A.K.M, T.P.E, and M.W. performed research, A.K.M., T.P.E., and M.W. analyzed data, A.K.M. and M.W. wrote the paper.

REFERENCES

Banerjee A, Marbach F, Anselmi F, Koh MS, Davis MB, da Silva PG, Delevich K, Oyibo HK, Gupta P, Li B, Albeanu DF (2015) An Interglomerular Circuit Gates Glomerular Output and Implements Gain Control in the Mouse Olfactory Bulb. Neuron 87:193–207.

Bathellier B, Buhl DL, Accolla R, Carleton A (2008) Dynamic Ensemble Odor Coding in the Mammalian Olfactory Bulb: Sensory Information at Different Timescales. Neuron 57:586–598.

Bozza T, McGann JP, Mombaerts P, Wachowiak M (2004) In vivo imaging of neuronal activity by targeted expression of a genetically encoded probe in the mouse. Neuron 42:9–21.

Brunert D, Tsuno Y, Rothermel M, Shipley MT, Wachowiak M (2016) Cell-Type-Specific Modulation of Sensory Responses in Olfactory Bulb Circuits by Serotonergic Projections from the Raphe Nuclei. J Neurosci 36:6820–6835.

Buck L, Axel R (1991) A novel multigene family may encode odorant receptors: a molecular basis for odor recognition. Cell 65:175–187.

Buonviso N, Amat C, Litaudon P, Roux S, Royet J-P, Farget V, Sicard G (2003) Rhythm sequence through the olfactory bulb layers during the time window of a respiratory cycle. Eur J Neurosci 17:1811–1819.

Burton SD (2017) Inhibitory circuits of the mammalian main olfactory bulb. J Neurophysiol 118:2034–2051.

Burton SD, Ermentrout GB, Urban NN (2012) Intrinsic heterogeneity in oscillatory dynamics limits correlation-induced neural synchronization. J Neurophysiol 108:2115–2133.

Burton SD, Wipfel M, Guo M, Eiting TP, Wachowiak M (2019) A novel olfactometer for efficient and flexible odorant delivery. Chem Senses 35:1521.

Carey RM, Verhagen JV, Wesson DW, Pírez N, Wachowiak M (2009) Temporal structure of receptor neuron input to the olfactory bulb imaged in behaving rats. J Neurophysiol 101:1073–1088.

Carey RM, Wachowiak M (2011) Effect of sniffing on the temporal structure of mitral/tufted cell output from the olfactory bulb. J Neurosci 31:10615–10626.

Charpak S, Mertz J, Beaurepaire E, Moreaux L, Delaney K (2001) Odor-evoked calcium signals in dendrites of rat mitral cells. Proc Natl Acad Sci USA 98:1230–1234.

Chen T-W, Wardill TJ, Sun Y, Pulver SR, Renninger SL, Baohan A, Schreiter ER, Kerr RA, Orger MB, Jayaraman V, Looger LL, Svoboda K, Kim DS (2013) Ultrasensitive fluorescent proteins for imaging neuronal activity. Nature 499:295–300.

Cleland TA, Linster C (2012) On-Center/Inhibitory-Surround Decorrelation via Intraglomerular Inhibition in the Olfactory Bulb Glomerular Layer. Front Integr Neurosci 6:5.

Dana H, Mohar B, Sun Y, Narayan S, Gordus A, Hasseman JP, Tsegaye G, Holt GT, Hu A, Walpita D, Patel R, Macklin JJ, Bargmann CI, Ahrens MB, Schreiter ER, Jayaraman V, Looger LL, Svoboda K, Kim DS (2016) Sensitive red protein calcium indicators for imaging neural activity. Elife 5:413.

De Saint Jan D, Hirnet D, Westbrook GL, Charpak S (2009) External tufted cells drive the output of olfactory bulb glomeruli. J Neurosci 29:2043–2052.

Debarbieux F, Audinat E, Charpak S (2003) Action potential propagation in dendrites of rat mitral cells in vivo. J Neurosci 23:5553–5560.

Díaz-Quesada M, Youngstrom IA, Tsuno Y, Hansen KR, Economo MN, Wachowiak M (2018) Inhalation Frequency Controls Reformatting of Mitral/Tufted Cell Odor Representations in the Olfactory Bulb. Journal of Neuroscience 38:2189–2206.

Djurisic M, Popovic M, Carnevale N, Zecevic D (2008) Functional structure of the mitral cell dendritic tuft in the rat olfactory bulb. J Neurosci 28:4057–4068.

Economo MN, Hansen KR, Wachowiak M (2016) Control of Mitral/Tufted Cell Output by Selective Inhibition among Olfactory Bulb Glomeruli. Neuron 91:397–411.

Eiting TP, Wachowiak M (2018) Artificial Inhalation Protocol in Adult Mice. Bio Protoc 8.

Geffen MN, Broome BM, Laurent G, Meister M (2009) Neural Encoding of Rapidly Fluctuating Odors. Neuron 61:570–586.

Geramita M, Urban NN (2017) Differences in Glomerular-Layer-Mediated Feedforward Inhibition onto Mitral and Tufted Cells Lead to Distinct Modes of Intensity Coding. J Neurosci 37:1428–1438.

Gire DH, Franks KM, Zak JD, Tanaka KF, Whitesell JD, Mulligan AA, Hen R, Schoppa NE (2012) Mitral cells in the olfactory bulb are mainly excited through a multistep signaling path. J Neurosci 32:2964–2975.

Gire DH, Schoppa NE (2009) Control of on/off glomerular signaling by a local GABAergic microcircuit in the olfactory bulb. J Neurosci 29:13454–13464.

Grobman M, Dalal T, Lavian H, Shmuel R, Belelovsky K, Xu F, Korngreen A, Haddad R (2018) A Mirror-Symmetric Excitatory Link Coordinates Odor Maps across Olfactory Bulbs and Enables Odor Perceptual Unity. Neuron 99:800–813.e806.

Haddad R, Lanjuin A, Madisen L, Zeng H, Murthy VN, Uchida N (2013) Olfactory cortical neurons read out a relative time code in the olfactory bulb. Nature Publishing Group 16:949–957.

Hallem EA, Carlson JR (2006) Coding of odors by a receptor repertoire. Cell 125:143–160.

Hayar A (2004) Olfactory Bulb Glomeruli: External Tufted Cells Intrinsically Burst at Theta Frequency and Are Entrained by Patterned Olfactory Input. Journal of Neuroscience 24:1190–1199.

Hayar A, Karnup S, Ennis M, Shipley MT (2004) External tufted cells: a major excitatory element that coordinates glomerular activity. J Neurosci 24:6676–6685.

Isaacson JS (1999) Glutamate spillover mediates excitatory transmission in the rat olfactory bulb. Neuron 23:377–384.

Isaacson JS, Strowbridge BW (1998) Olfactory reciprocal synapses: dendritic signaling in the CNS. Neuron 20:749–761.

Jordan R, Fukunaga I, Kollo M, Schaefer AT (2018) Active Sampling State Dynamically Enhances Olfactory Bulb Odor Representation. Neuron 98:1214–1228.e1215.

Lecoq J, Tiret P, Charpak S (2009) Peripheral Adaptation Codes for High Odor Concentration in Glomeruli. Journal of Neuroscience 29:3067–3072.

Liu S, Puche AC, Shipley MT (2016) The Interglomerular Circuit Potently Inhibits Olfactory Bulb Output Neurons by Both Direct and Indirect Pathways. J Neurosci 36:9604–9617.

Liu, R., Li, Z., Marvin, J. S. & Kleinfeld, D. (2019) Direct wavefront sensing enables functional imaging of infragranular axons and spines. Nat Meth 16, 615–618

Margrie TW, Sakmann B, Urban NN (2001) Action potential propagation in mitral cell lateral dendrites is decremental and controls recurrent and lateral inhibition in the mammalian olfactory bulb. Proc Natl Acad Sci USA 98:319–324.

Marvin JS et al. (2018) Stability, affinity, and chromatic variants of the glutamate sensor iGluSnFR. Nat Meth 15:936–939.

Marvin JS, Borghuis BG, Tian L, Cichon J, Harnett MT, Akerboom J, Gordus A, Renninger SL, Chen T-W, Bargmann CI, Orger MB, Schreiter ER, Demb JB, Gan W-B, Hires SA, Looger LL (2013) An optimized fluorescent probe for visualizing glutamate neurotransmission. Nat Meth 10:162–170.

Matsumoto H, Kashiwadani H, Nagao H, Aiba A, Mori K (2009) Odor-induced persistent discharge of mitral cells in the mouse olfactory bulb. J Neurophysiol 101:1890–1900.

McGann JP, Pírez N, Gainey MA, Muratore C, Elias AS, Wachowiak M (2005) Odorant representations are modulated by intra- but not interglomerular presynaptic inhibition of olfactory sensory neurons. Neuron 48:1039–1053.

Murphy GJ, Darcy DP, Isaacson JS (2005) Intraglomerular inhibition: signaling mechanisms of an olfactory microcircuit. Nat Neurosci 8:354–364.

Murphy GJ, Glickfeld LL, Balsen Z, Isaacson JS (2004) Sensory neuron signaling to the brain: properties of transmitter release from olfactory nerve terminals. J Neurosci 24:3023–3030.

Nagai Y, Sano H, Yokoi M (2005) Transgenic expression of Cre recombinase in mitral/tufted cells of the olfactory bulb. Genesis 43:12–16.

Najac M, De Saint Jan D, Reguero L, Grandes P, Charpak S (2011) Monosynaptic and polysynaptic feed-forward inputs to mitral cells from olfactory sensory neurons. J Neurosci 31:8722–8729.

Padmanabhan K, Urban NN (2010) Intrinsic biophysical diversity decorrelates neuronal firing while increasing information content. Nature Publishing Group 13:1276–1282.

Patriarchi T, Cho JR, Merten K, Howe MW, Marley A, Xiong W-H, Folk RW, Broussard GJ, Liang R, Jang MJ, Zhong H, Dombeck D, Zastrow von M, Nimmerjahn A, Gradinaru V, Williams JT, Tian L (2018) Ultrafast neuronal imaging of dopamine dynamics with designed genetically encoded sensors. Science 360:eaat4422.

Pologruto TA, Sabatini BL, Svoboda K (2003) ScanImage: flexible software for operating laser scanning microscopes. Biomed Eng Online 2:13.

Ressler KJ, Sullivan SL, Buck LB (1994) Information coding in the olfactory system: evidence for a stereotyped and highly organized epitope map in the olfactory bulb. Cell 79:1245–1255.

Richter FG, Fendl S, Haag J, Drews MS, Borst A (2018) Glutamate Signaling in the Fly Visual System. iScience 7:85–95.

Schaefer AT, Margrie TW (2007) Spatiotemporal representations in the olfactory system. Trends in Neurosciences 30:92–100.

Schoppa NE, Urban NN (2003) Dendritic processing within olfactory bulb circuits. Trends in Neurosciences 26:501–506.

Shao Z, Puche AC, Liu S, Shipley MT (2012) Intraglomerular inhibition shapes the strength and temporal structure of glomerular output. J Neurophysiol 108:782–793.

Short SM, Wachowiak M (2019) Temporal dynamics of inhalation-linked activity across defined subpopulations of mouse olfactory bulb neurons imaged in vivo. eNeuro:ENEURO.0189–19.2019.

Shusterman R, Smear MC, Koulakov AA, Rinberg D (2011) Precise olfactory responses tile the sniff cycle. Nature Publishing Group 14:1039–1044.

Spors H, Wachowiak M, Cohen LB, Friedrich RW (2006) Temporal dynamics and latency patterns of receptor neuron input to the olfactory bulb. J Neurosci 26:1247–1259.

Sun F et al. (2018) A Genetically Encoded Fluorescent Sensor Enables Rapid and Specific Detection of Dopamine in Flies, Fish, and Mice. Cell 174:481–496.e19.

Vaaga CE, Westbrook GL (2016) Parallel processing of afferent olfactory sensory information. J Physiol (Lond) 594:6715–6732.

Verhagen JV, Wesson DW, Netoff TI, White JA, Wachowiak M (2007) Sniffing controls an adaptive filter of sensory input to the olfactory bulb. Nat Neurosci 10:631–639.

Wachowiak M (2011) All in a sniff: olfaction as a model for active sensing. Neuron 71:962–973.

Wachowiak M, Cohen LB (2001) Representation of odorants by receptor neuron input to the mouse olfactory bulb. Neuron 32:723–735.

Wachowiak M, Shipley MT (2006) Coding and synaptic processing of sensory information in the glomerular layer of the olfactory bulb. Seminars in Cell & Developmental Biology 17:411–423.

Whitesell JD, Sorensen KA, Jarvie BC, Hentges ST, Schoppa NE (2013) Interglomerular lateral inhibition targeted on external tufted cells in the olfactory bulb. J Neurosci 33:1552–1563.

Wilson CD, Serrano GO, Koulakov AA, Rinberg D (2017) A primacy code for odor identity. Nat Commun 8:1477.

FIGURE LEGENDS

Figure 1. Characterization of iGluSnFRs as reporters of glutamatergic signaling onto MT cells.
A. Expression of SF-iGluSnFR.A184V in MT cells of the olfactory bulb. Top left: Expression of A184V variant across the length of the MT cell (white arrows) in an olfactory bulb injected animal. Bottom left: original iGluSnFR expression among EPL dendrites along the membrane surface.
B. Middle Top: Resting fluorescence image of the original iGluSnFR protein. Top right: ΔF response map to 8 presentations of ethyl butyrate during a 2Hz inhalation. Bottom Middle/Right: Responses across three glomeruli and zoom into first 2 seconds of the odor presentation.
C.Top: Raw and normalized ΔF/F responses of ITAs for all SF-variants. See Text for details. Bottom: Cumulative fraction of response magnitude across the population of significant G-O pairs for each variant.
D. mean RLI and ΔF of iGluSnFR (A184S) signal imaged at high zoom in several glomeruli. Note lack of signal on apical dendrites or somata of MT cells.
E. iGluSnFR signals from difference MT cellular compartments
F. Left: Glutamate input onto lateral dendrites of MT cells across two odorants. Right: Odorant-evoked, excitatory and putative suppressive glutamate responses in lateral dendrites using SF-iGluSnFR.A184S.

Figure 2. Glomerular glutamate responses show temporally diverse inhalation-driven dynamics.
A. Left) Mean fluorescence of A184V across MT cells in the OB. Right) Inhalation-triggered average (ITA) ΔF maps of across three odorants (ethyl butyrate, methyl tiglate, 2-hexanone).
B. Averaged ITA response traces across 3 odorants. Left: ITA of ROI5 across 3 odorants. Right: Responses of individual glomeruli across each odorant.
C. Onset latency, time to peak, and duration of all ITA G-O pairs across 5 fields of view.
D. Cumulative fraction of median-subtracted, ITA onset latencies for iGluSnFR data, compared to that of GCaMP6f signals in OSN axon terminals (data taken from Short & Wachowiak, 2019).

Figure 3. Diversity of temporal patterns of glutamatergic signaling across repeated samples of odorant.
A. Mean fluorescence and odorant-evoked ΔF maps for 13 odorants imaged with SF-iGluSnFR-A184S.
B. Time-series of iGluSnFR signal from 4 glomerular ROIs, showing continuous signal over 3 odor presentations of 12 odorants presented in random order. Vertical line indicates time of odorant onset. Odorant duration, 2 seconds. Signal is low-pass filtered at 0.5 Hz for display.
C. Averaged odor-evoked responses for 4 odorants. Inset: Correlation to 1st inhalation across all ROIs (time bins = 0.386s).

D. Proportion of excitatory (Exc.), suppressive (Sup) and biphasic (Exc. & Sup.) responses across the responsive population and the entire population of ROIs.
E. Average correlation ± SEM to response pattern immediately after odorant onset, for five time bins spanning the duration of odor presentation. Right: Range of correlation coefficients for each odorant. See Text for details.

Figure 4. Odorant concentration leads to systematic and nonlinear changes in glutamate signaling onto MT cells.
A. Waterfall plots (left) and time-courses from select glomeruli (right) showing iGluSnFR signals in response to 3 concentrations of odorant for three different odorants. All data are from the same experiment and field of view. Only glomeruli showing significant responses at all 3 concentrations are shown. Inhalation frequency, 2 Hz; odorant duration, 4 seconds.
B. Change in iGluSnFR response amplitude from beginning to end of odorant presentation ($T2-T1/T_{max}$; see Text for details), calculated for 5 odorants tested across 3 concentrations (in 4 mice). Inset illustrates definition of the measure.
C. Coherence of iGluSnFR signal to the 2Hz inhalation frequency, measured for each concentration, for the same dataset.
D. Coherence values for individual glomerulus-odorant pairs comparing the lowest (1x) and highest (10x) concentrations, and color-coded for each odorant. Note lack of reduction in coherence for 2-hexanone.

Figure 5. Correspondence between glutamate and calcium transients in MT cells of the same glomerulus revealed by dual-color imaging.
A. Post-hoc histology highlighting jRGECO1a and SF-iGluSnFR expression in MT cells. green arrow: membrane expression of SF-iGluSnFR, magenta arrow: jRGECO1a cytoplasmic expression.
B. Mean iGluSnFR (A184S) fluorescence and odorant-evoked ΔF response maps for A184S and jRGECO signals, along with traces showing the signal time-course in each channel. Odorant is isobutylthiazole. Note jRGECO signal in dendrites of several MT cells exiting the central glomerulus. Traces show responses from this glomerulus and two dendrites.
C. iGluSnFR and jRGECO response maps for 4 odorants, showing high correspondence in response. Left images show mean fluorescence maps across both channels.
D. Traces showing continuous dual-color recording across 11 consecutive odorant presentations, taken from two glomeruli, showing high correspondence in iGluSnFR and jRGECO signals despite diverse temporal patterns of response to different odorants. Glomerulus 2 (lower traces) shows clear suppressive components in both signals. Asterisks denote a biphasic response in glutamate signal that is not present in the calcium signal.
E. Average calcium and glutamate responses across 4 presentations of 5 odorants and 3 ROIs, taken from the preparation in (C), illustrating high correspondence in response dynamics.

Figure 6. Diversity of glutamate dynamics imaged from MT cells in the awake mouse.

A. Mean iGluSnFR (A184V) fluorescence and ΔF response map from the dorsal OB of an awake, head-fixed mouse.

B. Glutamate signals taken from 3 glomeruli in a single presentation of odorant. Top trace shows respiration/sniffing as measured with an external flow sensor. Lower left shows snippet of signals from each glomerulus, illustrating temporal lag between different glomeruli and consistency of dynamics with each sniff. Signals are unfiltered. Lower right shows ITA waveforms for each glomerulus, generated across 137 sniffs over 6 trials of ethyl butyrate (see Methods for details). Vertical line indicates time of inhalation onset.

C. Time-dependent decorrelation and nonlinear effect of odorant concentration on glutamate signals in the awake mouse. Traces shows signals from 3 glomeruli, averaged over 4 trials, in response to a low (1:1000 liquid dilution) and high (1:10 dilution) concentration of ethyl tiglate. Note strong adaptation apparent in ROI 1 and facilitation in ROIs 2 and 3.

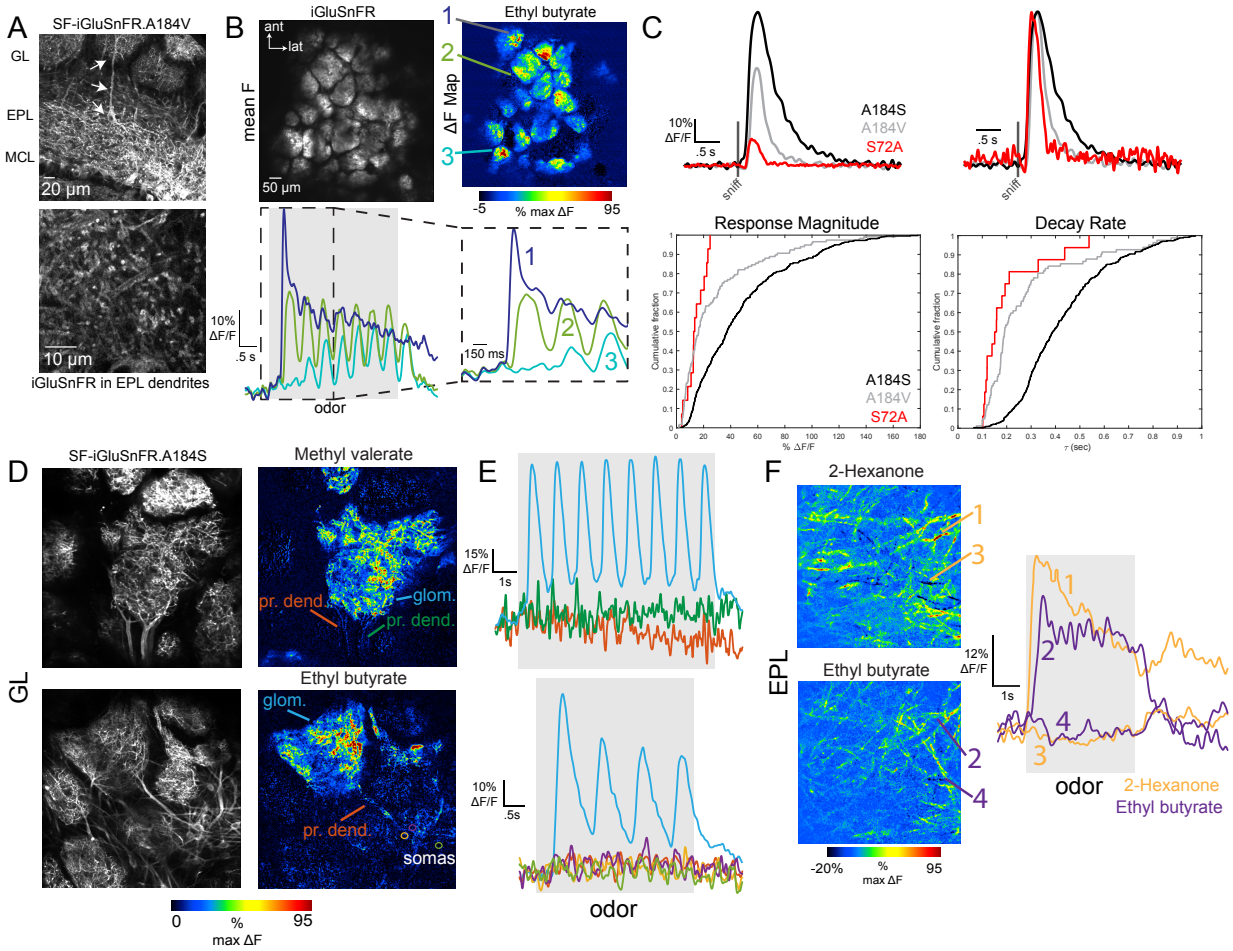

Figure 1. Characterization of iGluSnFRs as reporters of glutamatergic signaling onto MT cells.

A. Expression of SF-iGluSnFR.A184V in MT cells of the olfactory bulb. Top left: Expression of A184V variant across the length of the MT cell (white arrows) in an olfactory bulb injected animal. Bottom left: original iGluSnFR expression among EPL dendrites along the membrane surface.
B. Middle Top: Resting fluorescence image of the original iGluSnFR protein. Top right: ΔF response map to 8 presentations of ethyl butyrate during a 2Hz inhalation. Bottom Middle/Right: Responses across three glomeruli and zoom into first 2 seconds of the odor presentation.
C.Top: Raw and normalized ΔF/F responses of ITAs for all SF-variants. See Text for details. Bottom: Cumulative fraction of response magnitude across the population of significant G-O pairs for each variant.
D. mean RLI and ΔF of iGluSnFR (A184S) signal imaged at high zoom in several glomeruli. Note lack of signal on apical dendrites or somata of MT cells.
E. iGluSnFR signals from different MT cellular compartments.
F. Left: Glutamate input onto lateral dendrites of MT cells across two odorants. Right: Odorant-evoked, excitatory and putative suppressive glutamate responses in lateral dendrites using SF-iGluSnFR.A184S.

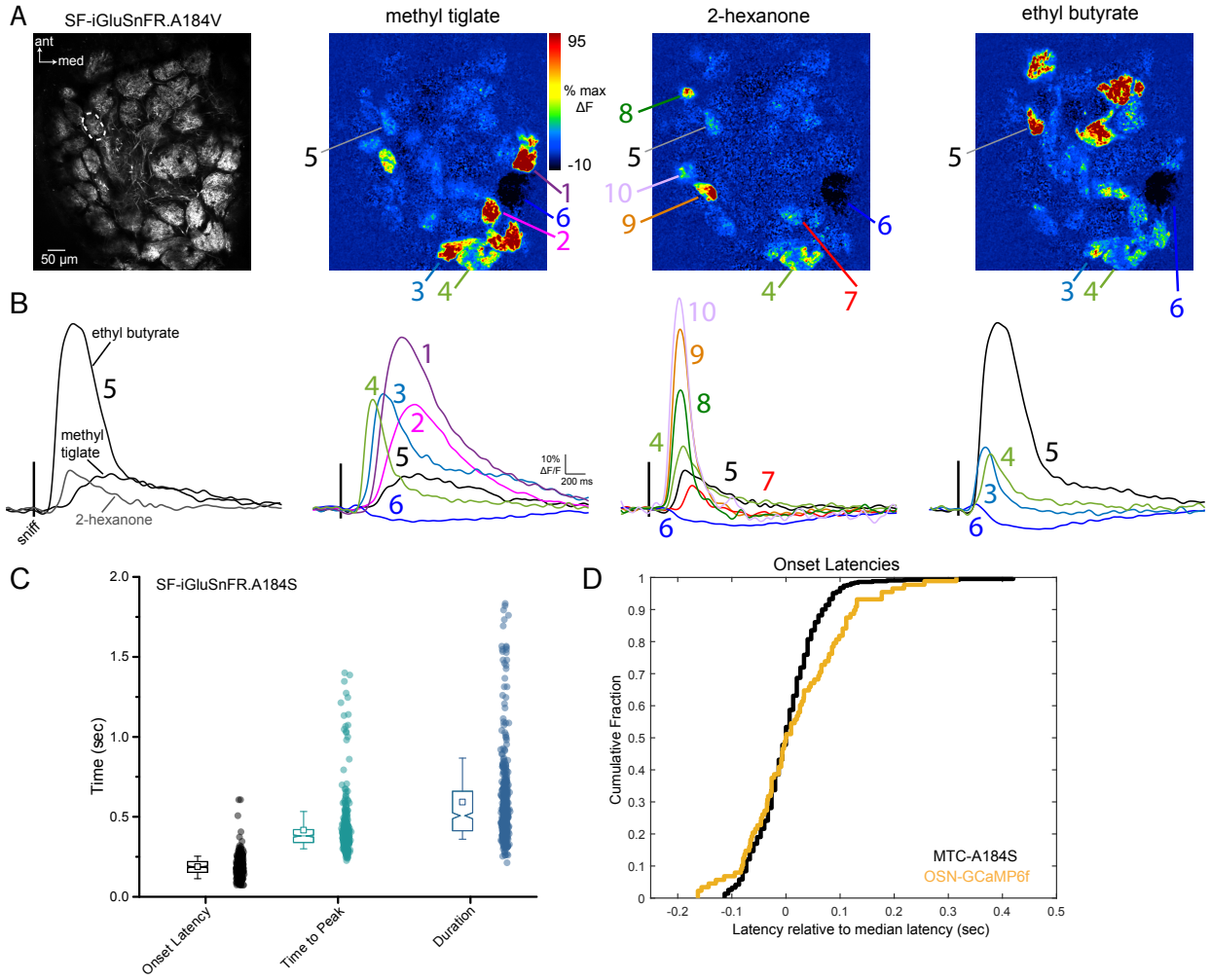

Figure 2. Glomerular glutamate responses show temporally diverse inhalation-driven dynamics.

A. Left) Mean fluorescence of A184V across MT cells in the OB. Right) Inhalation-triggered average (ITA) ΔF maps of across three odorants (ethyl butyrate, methyl tiglate, 2-hexanone).
B. Averaged ITA response traces across 3 odorants. Left: ITA of ROI5 across 3 odorants. Right: Responses of individual glomeruli across each odorant.
C. Onset latency, time to peak, and duration of all ITA G-O pairs across 5 fields of view.
D. Cumulative fraction of median-subtracted, ITA onset latencies for iGluSnFR data, compared to that of GCaMP6f signals in OSN axon teminals (data taken from Short & Wachowiak, 2019).

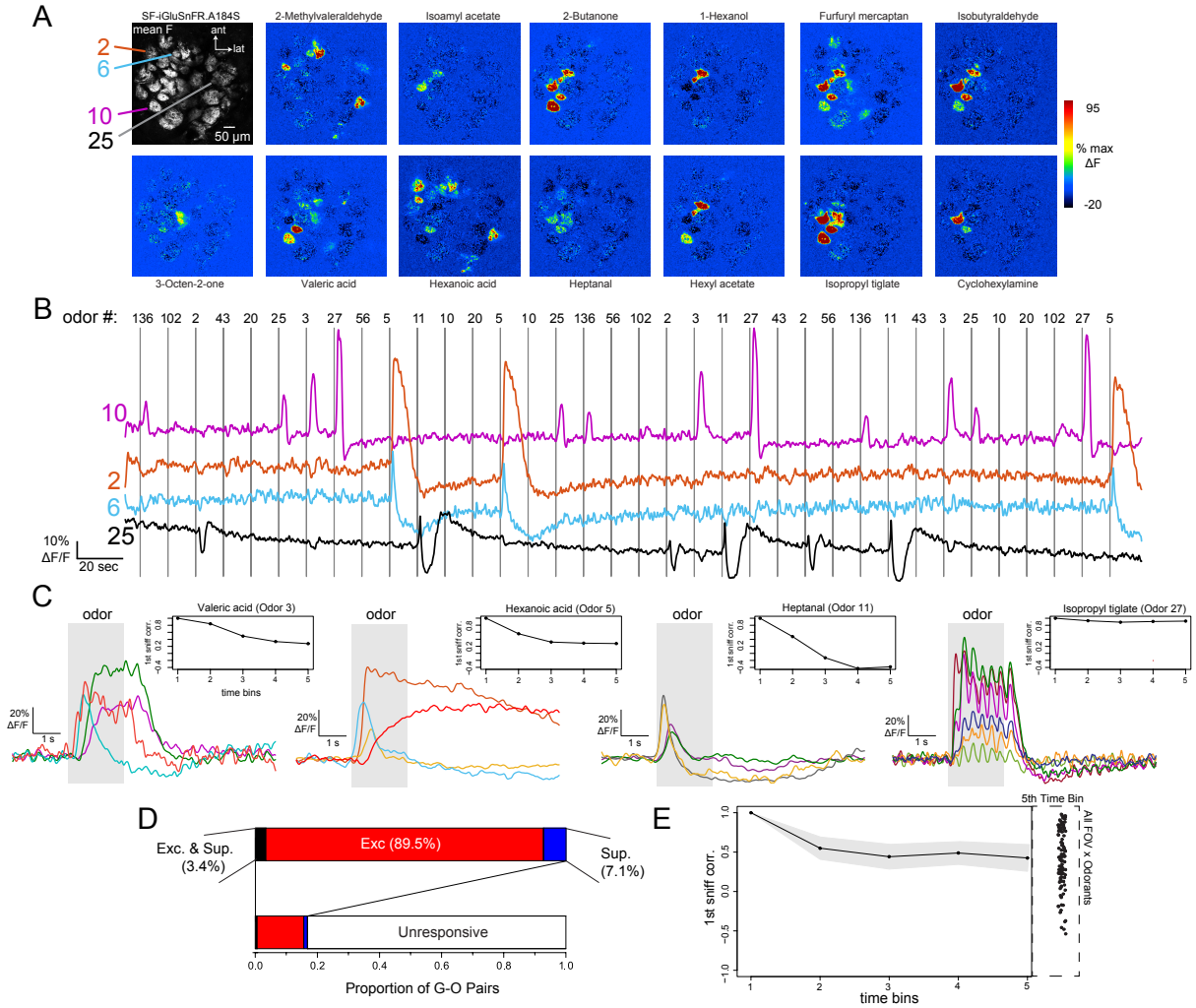

Figure 3. Diversity of temporal patterns of glutamatergic signaling across repeated samples of odorant.

A. Mean fluorescence and odorant-evoked ΔF maps for 13 odorants imaged with SF-iGluSnFR-A184S.
B. Time-series of iGluSnFR signal from 4 glomerular ROIs, showing continuous signal over 3 odor presentations of 12 odorants presented in random order. Vertical line indicates time of odorant onset. Odorant duration, 2 seconds. Signal is low-pass filtered at 0.5 Hz for display.
C. Averaged odor-evoked responses for 4 odorants. Inset: Correlation to 1st inhalation across all ROIs (time bins = 0.386s).
D. Proportion of excitatory (Exc.), suppressive (Sup) and biphasic (Exc. & Sup.) responses across the responsive population and the entire population of ROIs.
E. Average correlation ± SEM to response pattern immediately after odorant onset, for five time bins spanning the duration of odor presentation. Right: Range of correlation coefficients for each odorant. See Text for details.

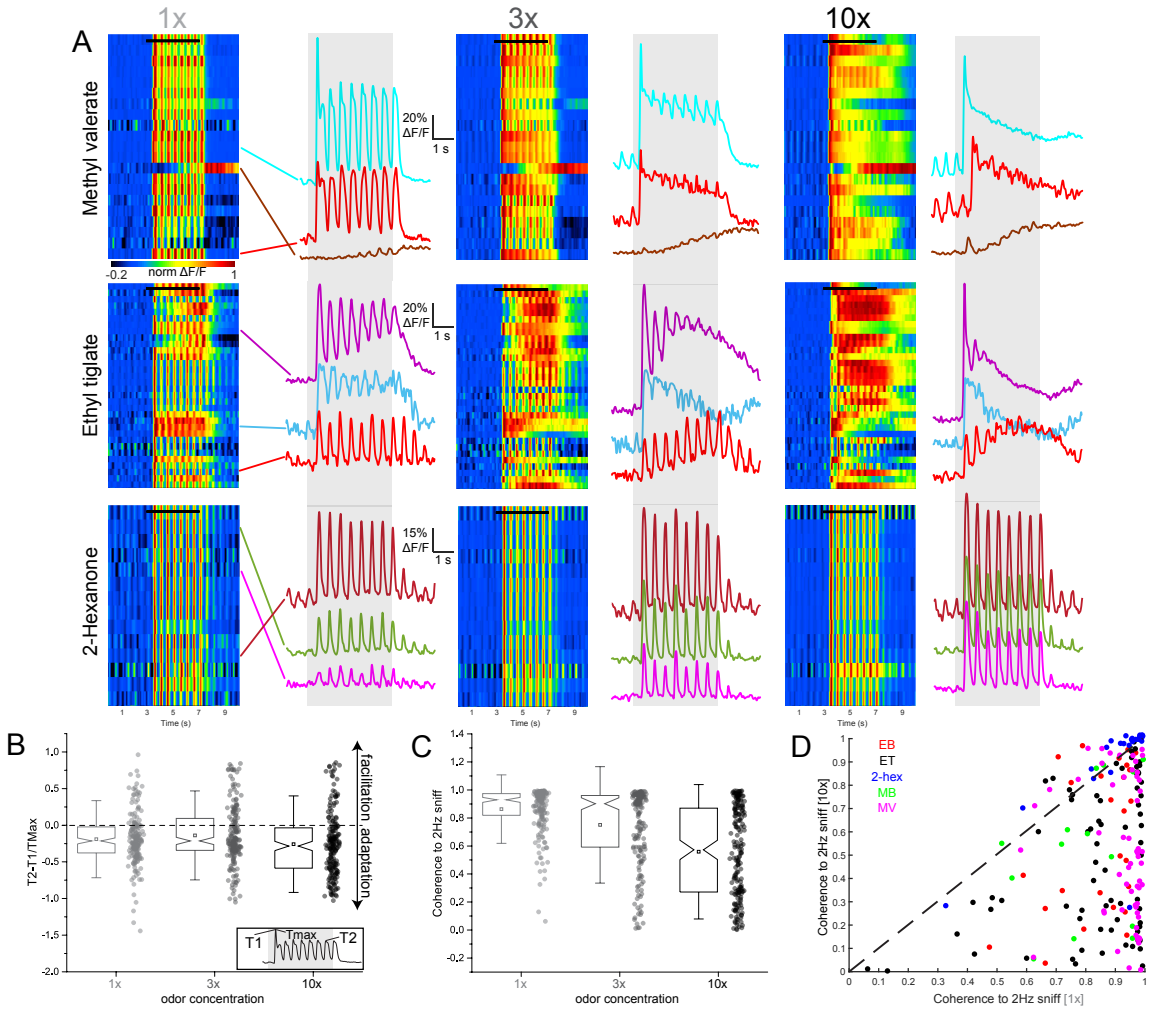

Figure 4. Odorant concentration leads to systematic and nonlinear changes in glutamate signaling onto MT cells.

A. Waterfall plots (left) and time-courses from select glomeruli (right) showing iGluSnFR signals in response to 3 concentrations of odorant for three different odorants. All data are from the same experiment and field of view. Only glomeruli showing significant responses at all 3 concentrations are shown. Inhalation frequency, 2 Hz; odorant duration, 4 seconds.
B. Change in iGluSnFR response amplitude from beginning to end of odorant presentation (T2-T1/Tmax; see Text for details), calculated for 5 odorants tested across 3 concentrations (in 4 mice). Inset illustrates definition of the measure.
C. Coherence of iGluSnFR signal to the 2Hz inahaltion frequency, measured for each concentration, for the same dataset.
D. Coherence values for individual glomerulus-odorant pairs comparing the lowest (1x) and highest (10x) concentrations, and color-coded for each odorant. Note lack of reduction in coherence for 2-hexanone.

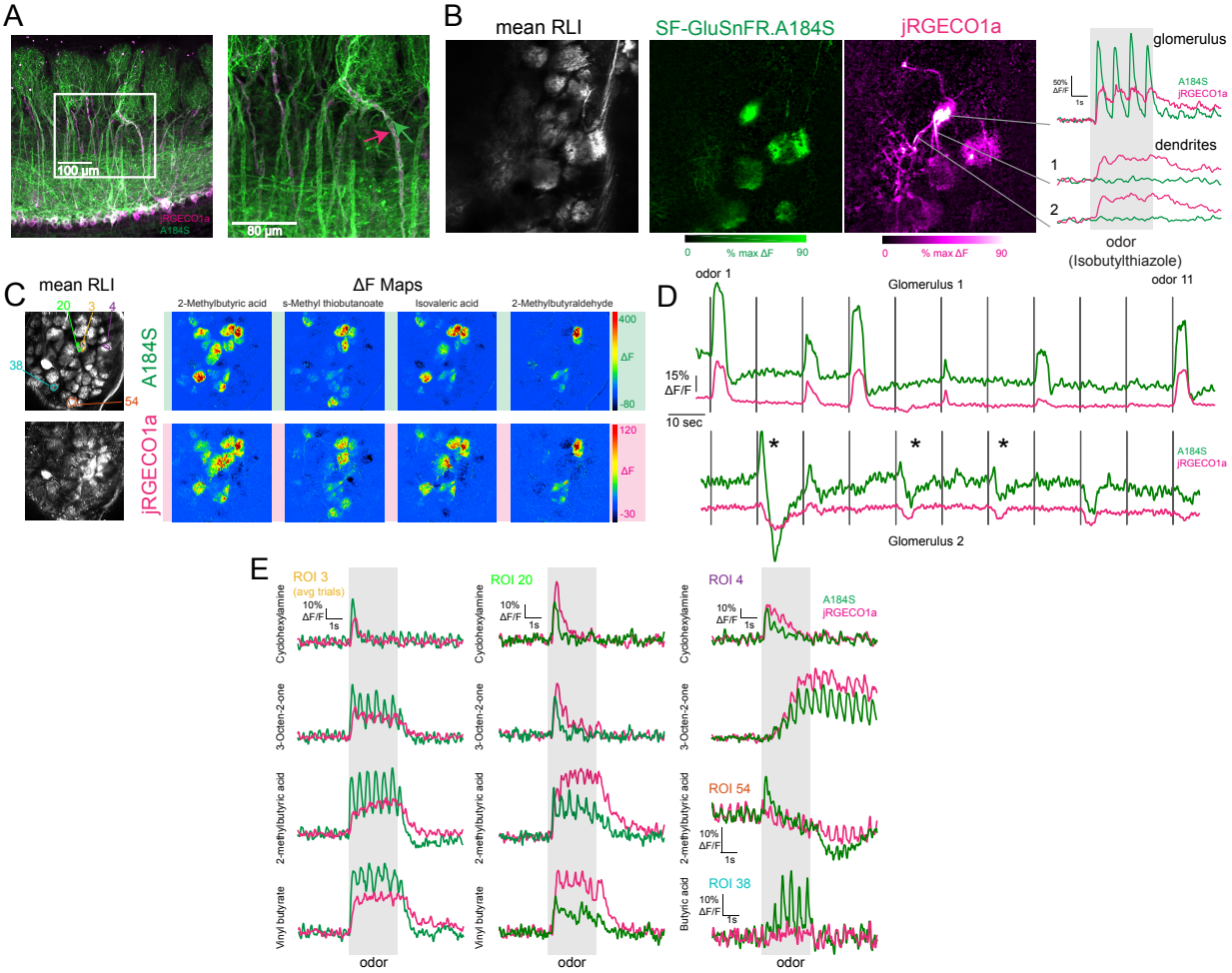

Figure 5. Correspondence between glutamate and calcium transients in MT cells of the same glomerulus revealed by dual-color imaging.

A. Post-hoc histology highlighting jRGECO1a and SF-iGluSnFR expression in MT cells. green arrow: membrane expression of SF-iGluSnFR, magenta arrow: jRGECO1a cytoplasmic expression.
B. Mean iGluSnFR (A184S) fluorescence and odorant-evoked ΔF response maps for A184S and jRGECO signals, along with traces showing the signal time-course in each channel. Odorant is isobutylthiazole. Note jRGECO signal in dendrites of several MT cells exiting the central glomerulus. Traces show responses from this glomerulus and two dendrites.
C. iGluSnFR and jRGECO response maps for 4 odorants, showing high correspondence in response. Left images show mean fluorescence maps across both channels.
D. Traces showing continuous dual-color recording across 11 consecutive odorant presentations, taken from two glomeruli, showing high correspondence in iGluSnFR and jRGECO signals despite diverse temporal patterns of response to different odorants. Glomerulus 2 (lower traces) shows clear suppressive components in both signals. Asterisks denote a biphasic response in glutamate signal that is not present in the calcium signal.
E. Average calcium and glutamate responses across 4 presentations of 5 odorants and 3 ROIs, taken from the preparation in (C), ilustrating high correspondence in repsonse dynamics.

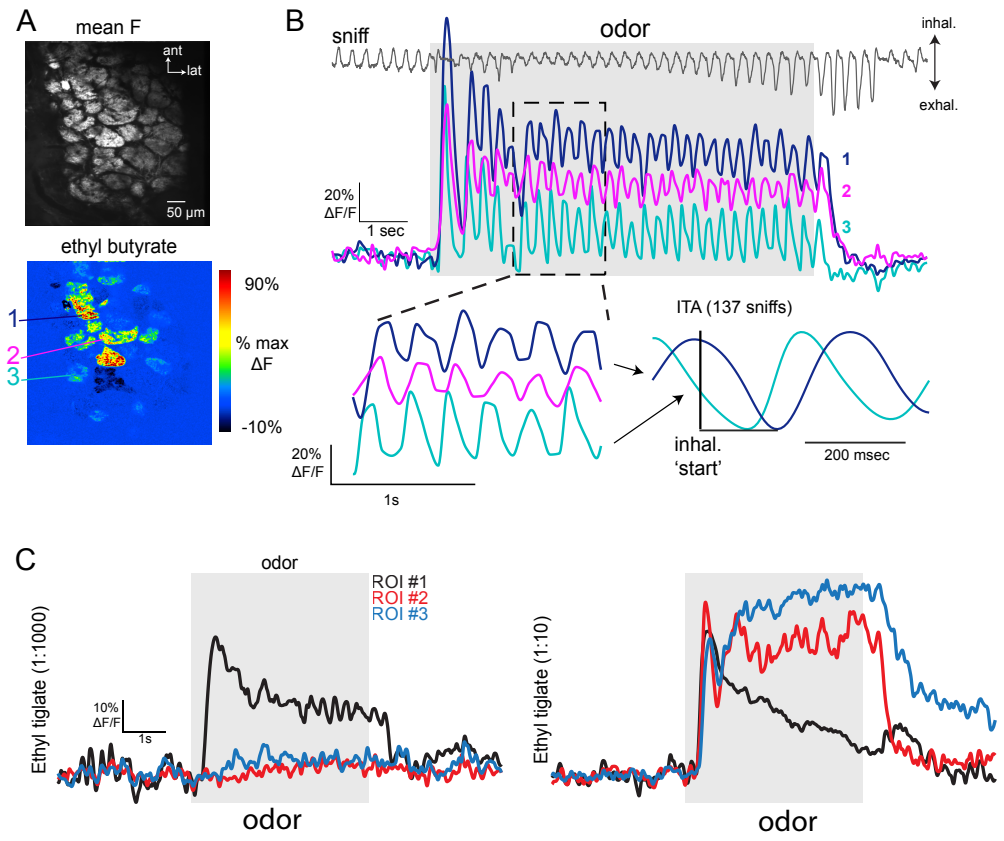

Figure 6. Diversity of glutamate dynamics imaged from MT cells in the awake mouse.

A. Mean iGluSnFR (A184V) fluorescence and ΔF response map fromthe dorsal OB of an awake, head-fixed mouse.
B. Glutamate signals taken from 3 glomeruli in a single presentation of odorant. Top trace shows respiration/sniffing as measured with an external flow sensor. Lower left shows snippet of signals from each glomerulus, illustrating temporal lag between different glomeruli and consistency of dynamics with each sniff. Signals are unfiltered. Lower right shows ITA waveforms for each glomerulus, generated across 137 sniffs over 6 trials of ethyl butyrate (see Methods for details). Vertical line indicates time of inhalation onset.
C. Time-dependent decorrelation and nonlinear effect of odorant concentration on glutamate signals in the awake mouse. Traces shows signals from 3 glomeruli, averaged over 4 trials, in response to a low (1:1000 liquid dilution) and high (1:10 dilution) concentration of ethyl tiglate. Note strong adaptation apparent in ROI 1 and facilitation in ROIs 2 and 3.